IEEE Access
Multidisciplinary | Rapid Review | Open Access Journal

Date of publication xxxx 00, 0000, date of current version xxxx 00, 0000.

Digital Object Identifier 10.1109/ACCESS.2017.Doi Number

Time - altitude variation of 30-second-update full volume scan data for summer convective storms observed with X-band dual polarized phased array weather radar

Hiroshi Kikuchi[1]*, (Member, IEEE), Yasuhide Hobara[1,2], and Tomoo Ushio[3], (Senior Member, IEEE)

[1]Center for Space Science and Radio Engineering (SSRE), The University of Electro Communications, Chofu,Tokyo, 182-8585, Japan.
[2]Graduate School of Informatics and Engineering, The University of Electro Communications, Chofu,Tokyo, 182-8585, Japan.
[3]Graduate School of Engineering, Osaka University, Suita, Osaka 565-0871, Japan.

Corresponding Author: Hiroshi Kikuchi (mail: hkikuchi@uec.ac.jp)

This work was finacially supported by JSPS KAKENHI Grant Number 22K04121.

ABSTRACT Dual-polarization radars with parabolic dish antennas, which transmit horizontal and vertical waves, are widely used to measure precipitation. However, such radars cannot properly observe the convective storms developing at high altitudes in a short time because of the low spatiotemporal resolution of the data due to mechanical scanning at azimuth and elevation angles. In 2018, an X-band dual-polarized phased array weather radar (DP-PAWR) was developed in Japan. DP-PAWR provides polarimetric precipitation measurements via three dimentional (3D) volume scanning in 30 s using electronic scanning at elevation angles. This study investigated the relationship between the amount of full volume scan data (the radar reflectivity factor(Z_h), differential reflectivity(Z_{dr}), and specific differential phase(K_{dp})) above the freezing level and that of near-surface rainfall for three characteristically different summer convective storms in Japan. We also discussed the quantitative predictability of near-surface rainfall volume using the full volume scan data above the freezing level obtained from DP-PAWR. The results showed that the 30-s full volume scan data above the freezing level can quantitatively predict near-surface rainfall volume for various storms, including heavy convective storms multi-precipitation cores, as well as small-scale convective storms with 5 to 11.5 minutes of lead-time.

INDEX TERMS Weather radar, precipitaion obsevation, full volume scan data.

I. INTRODUCTION

In recent years, a range of weather radars has found application in various fields, with ongoing hardware development efforts. Notable recent examples encompass radars designed to observe cloud scatters, including aircraft-mounted radar [1], radar systems mounted on unmanned aerial vehicles [2], and dual-polarization radar systems on satellites [3].

Particularly, weather radar serves as an effective method for observing rainfall and providing effective information for disaster mitigation. Dual-polarization radars, which transmit both horizontal and vertical polarized waves, are widely utilized for measuring precipitation, serving both academic and practical purposes [4–8]. These radars capture returning waves, providing horizontal and vertical measurements of scatterers within clouds, such as raindrops, ice, and graupel. Consequently, dual-polarization variables offer more accurate estimates of rainfall rates and efficiently classify the particles in storms.

The radar variables using dual-polarization radars include the radar reflectivity factor (Z_h), differential reflectivity (Z_{dr}), differential phase (φ_{dp}), specific differential phase (K_{dp}), correlation coefficient (ρ_{hv}), and Doppler velocity, among others. Z_h ,which is also observable by single polarization radar is proportional to the size (or diameter) and the density of hydrometeors in the resolution volume and is used to estimate rainfall rates. Z_{dr} and K_{dp} columns, which are vertically extended regions of positive Z_{dr} and K_{dp} above the freezing

level, are often associated with the updrafts of convective storms [9–13] or supercells [14–17]. These signatures result from supercooled liquid drops or water-coated hailstones lifted several kilometers above the freezing level. In these previous studies, dual-polarization radars with parabolic dish antennas have been employed.

In Japan, 40 X or C-band dual polarized radars that also use a parabolic dish antenna are operated around urban areas. The radar can accurately estimate the rain rate using polarimetric and network observations. The temporal resolution of the radar is 1 min for low elevation angles (< 1°) and 5 min for elevations of 1°–15° [18–19]. In general, a weather radar uses a parabolic dish antenna that requires more than 5 min for the 3D observation due to mechanical rotation in both the azimuth and elevation angles. The number of observable elevation angles is approximately over a dozen. Consequently, these radars with a parabolic dish antenna are only able to conduct sparse observations at higher altitudes. Convective summer storms often develop over a dozen kilometers in a few minutes, bringing torrential rainfall within minutes of their onset. For rapidly developing convective clouds, the temporal resolution and observation density of parabolic weather radars, particularly at high altitudes, are frequently insufficient.

To improve the low spatiotemporal resolution, recent studies have focused on using a phased array antenna for conducting precipitation observations [e.g., 20–27]. In Japan, a dual polarized phased array weather radar (DP-PAWR) was developed in 2018 [28–29]. It is an X-band radar with an operating frequency of 9.425 GHz, and its scanning scheme involves mechanical and electronic scanning at azimuth and elevation angles, respectively. The DP-PAWR is capable of conducting precipitation measurements using dual-polarimetric observations for 3D volume scanning within a 60 km observation range in just 30 s.

Furthermore, the DP-PAWR captures 113 observations in the elevation direction and is capable of observing precipitation at high altitudes. It provides 30-s updates from which the volume (in km^3) of Z_h, Z_{dr}, and K_{dp}, can be calculated owing to its rapid and high-density observations. There have been no prior studies exploring the relationship between such high-density radar data at high altitudes and near-surface rainfall.

The purpose of this study is to investigate the relationship between the full volume scan data (Z_h, Z_{dr}, and K_{dp}) above the freezing level and near-surface rainfall during summer convective storms, utilizing DP-PAWR. We aim to assess the quantitative predictability of near-surface rainfall volume using the full volume scan data obtained from DP-PAWR.

TABLE 1
SPECIFICATIONS OF THE DP-PAWR.

Frequency (GHz)	9.425
Azimuth resolution (°)	1.2
Elevation resolution (°)	< 1.0
Observational range (km)	60
Observational elevation (°)	0–90
Temporal resolution for volume scan (s)	30
Range resolution (m)	75
No. of transmitted fan beams (Elevation angles; °)	7 (0–6;6–13;13–23;23–33;33–46;46–63;63–90)
No. of elevation angles	113

II. METHODOLGY

A. DUAL-POLARIZED PHASED ARRAY WEATHER RADAR (DP-PAWR)

The DP-PAWR provides rapid scanning and high-density observations. It uses a transmitted wave frequency center of 9.425 GHz, which is within the X-band. The transmitted waves of the DP-PAWR have wide beam widths with elevation angles of 6°–27° and a beam width at an azimuth angle of 1.2°. The wide transmitted beam is referred to as fan beam in this study. To cover the observation range in the elevation angles from 0° to 90°, 7 fan beams are simultaneously transmitted at each elevation angle [28]. The phased-array antenna comprises tandemly arranged 112 antenna elements for electronic scanning of the elevation angles with half-wavelengths (i.e., 16 mm). The width of the received beam after conducting the digital beamforming at the elevation angle is slightly less than 1.0 °. Consequently, the full volume scan data are obtained every 30 sec. Table 1 presents the specification of the DP-PAWR. In this study, the radar variables of Z_h, Z_{dr}, and K_{dp} are used to obain the volume data of a storm.

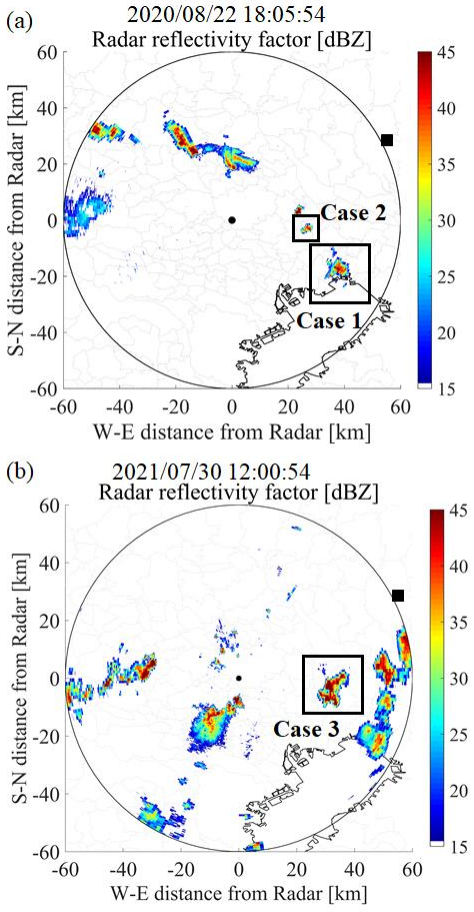

FIGURE 1. Example of the radar reflectivity factor in PPI image on August 22 in 2020(a) and July 30, 2021(b). Square dot indicate the observation site of the radio sonde.

B. ANALYTICAL METHODS AND A REVIEW OF CASE STUDIES

To explore the relationship between Z_h, Z_{dr}, and K_{dp} above the freezing level and near-surface rainfall, we computed the volume (in km^3) of these radar variables within each 30 s interval. The data above the freezing level is used to calculate the volume of radar variables using full scan data every 30 sec with DP-PAWR. We then compared this volume with the volume of Z_h below 2 km altitude to represent the amount of near-surface rainfall. The DP-PAWR's observation range includes urban areas, such as Tokyo city, which are prone to ground clutter due to tall buildings. Consequently, data at low altitudes (e.g., 1 km or less) are often missing. For this reason, we utilized data at altitudes of 2 km or less when calculating near-surface rainfall. The volumes (in km^3) of Z_h, Z_{dr}, and K_{dp} at > 45 dBZ, 3 dB, and 3 °/km, respectively, were calculated. In this paper, the threshold value of K_{dp} was set to 3 deg/km. This is based on the results of precipitation cores observed in a previous study [28]. In addition, some previous studies using other S-band radars have used values, such as 1 or 2 deg/km to obtain the signatures of K_{dp} but this paper uses 3 deg/km in consideration of the difference in observation frequency [31–33].

In this paper, we studied three characteristically different summer convective storms that were observed by the DP-PAWR in 2020 and 2021.

Fig.1 shows the plan position indicator (PPI) image of the Z_h for the analyzed cases obtained at an elevation angle of 2.4° using the DP-PAWR. The storms of case 1 and 2 occured almost spatiotemporally simultaneously on August 22, 2020, and were located only several tens of kilometers from each other. The storm of case 3 occured on July 30, 2021. In case 1, the horizontal scale of the storm was about 10−15 km. The highest echo top of the radar reflectivity of 45 dBZ was 9 km.

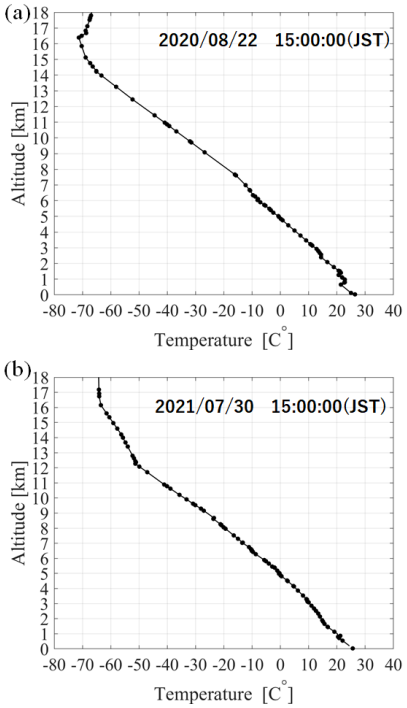

FIGURE 2. Temperature data from radio-sonde observations at 15:00 (JST) on August 22, 2020(a) and July 30, 2021(b).

The storm duration is 80 min. In case 2, the maximum echo top of 45 dBZ was 6 km, and its horizontal scale was 2 km. The storm duration is 30 min. In case 3, the horizontal scale of the storm was about 10 km. Similar to case 1, this case was a well-developed stom. The highest echo top of 45 dBZ and storm duration are 7 km and 90 min, respectively.

To define the altitude of the freezing level, the temperature data from radio-sonde observations of the upper atmosphere conducted by the Japan Meteorological Agency were used. Fig.

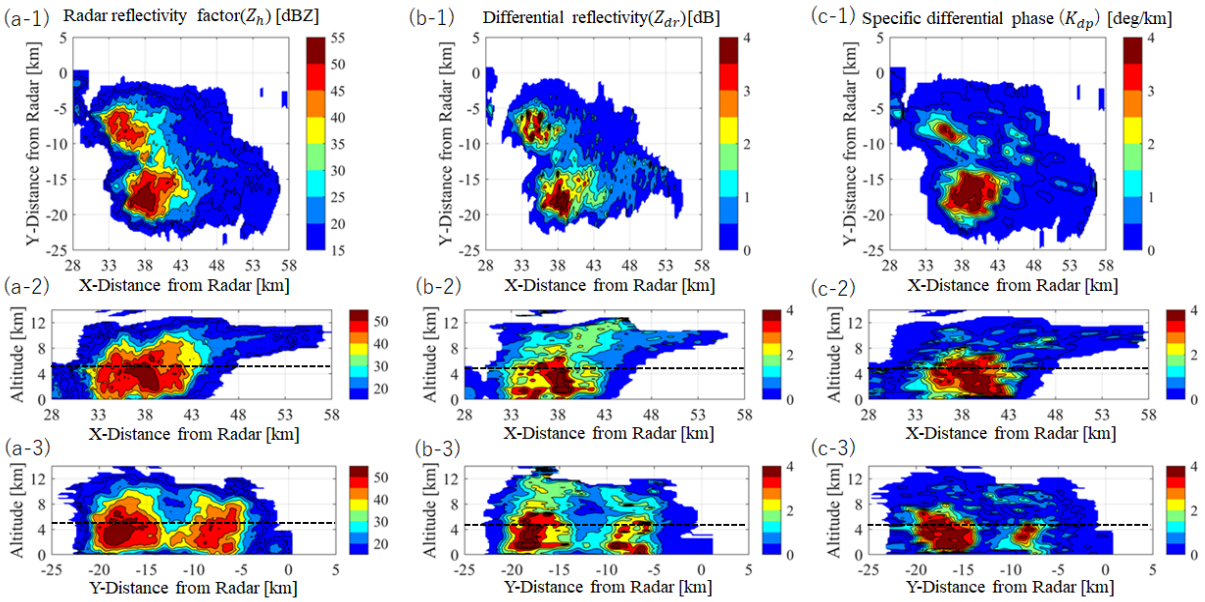

FIGURE 3. 3D distribution of the radar variables of Z_h, Z_{dr}, and K_{dp}. Panels (a), (b), and (c) show the maximum values of Z_h, Z_{dr}, and K_{dp} along a direction, respectively. The numbers 1, 2, and 3 indicate the maximum values across the vertical and horizontal direction. The dashed line indicates the freezing level considering the discussion using Fig. 4.

2 illustrates the temperature data from the Tateno observation site, situated at 36.0583° north latitude and 140.125° east longitude, as depicted in the square dot in Fig. 1. A radio-sonde was launched at 15:00 (Japan Standard Time; JST) on August 22, 2020, and July 30, 2021 and the results indicated that the freezing level, marked by a temperature of 0°C, was at approximately 5 km in both cases. The distance between the radio-sonde observation locations and the storms of case 1, 2, and 3 was approximately 51 km, 42 km, and 40 km, respectively.

III. RESULTS AND DISCUSSION

A. CASE 1

To understand the characteriscis of the storm in case 1, the three-dimentional distribution of the radar variables of Z_h, Z_{dr}, and K_{dp} obtained by DP-PAWR at 18:24:54 (JST) are shown in Fig. 3. Labels (a), (b), and (c) show the maximum values of the Z_h, Z_{dr}, and K_{dp} along each direction, respectively. The numbers 1, 2, and 3 signify the maximum values across the vertical direction (Z) of the altitude (from 0 to 13 km) for all XY locations, y (west-east)-the horizontal direction from -25 to 5 km for all XZ locations, and x(south-north)-the horizontal direction from 28 to 58 km for all YZ locations, respectively. The storm was observed from 18:00:24 to 19:15:24 on August 22, 2020. The horizontal scale of the storm was 10–15 km, as shown in panel (a-1). Two precipitation cores were observed in the analysis range. During the observation period, the precipitation core repeatedly developed at 38 and -18 km in x and y coordinates, respectively, and was advected northwestwards by the environmental winds. Such precipitation cores that occur more than once at the same location are more likely to cause precipitation disasters because of a large amount of near-surface rainfall.

In panels (a-2,3), the echo top at 45 dBZ was found to reach an altitude of 9 km. The vertical structure of Z_h, Z_{dr}, and K_{dp} ,clearly highlighted the precipitation core's presence in panels (a-2,3), (b-2,3), and (c-2,3), particularly in areas with high convective activity. In this case, the signature of the melting layer was not distinctly discernible using the polarimetric variables. To accurately estimate the freezing level in this case, ρ_{hv} data are used. Although ρ_{hv} for most meteorological echoes tends to be greater than 0.9, it can dip to be approximately 0.7 when melting hail and snowflakes are present near the melting layer. Therefore ρ_{hv} is useful to detect the freezing level.

Fig. 4 shows the vertical structure of ρ_{hv} at the same time as Fig. 3. Panels (a) and (b) are slices of the XZ and YZ planes at Y of -18 km and X of 38 km, respectively. From these figures, the ρ_{hv} is partially low at the altitude of 4.5 km with a black oval in panel (a). Therefore, in this study, the freezing level is set at 4.5 km, which is slightly lower than the radio-sonde data from Fig. 2.

Fig. 5 depicts the temporal evolution of the volume of Z_h below 2 km altitude, as well as Z_h, Z_{dr}, and K_{dp} above the freezing level in panels (a), (b), (c), and (d), respectively. In panel (a), the volume of near-surface rainfall increased between 18:20:54 and 19:10:54. This increase and decrease in rainfall volume were associated with the repeated development of precipitation cores, and after 18:43:24, the Z_h volume decreased as the updraft within the storms gradually weakened. Panels (b), (c), and (d) show that the peak values for Z_h, Z_{dr}, and K_{dp} volumes above the freezing level occurred around 18:25:54. These results suggest that all these variables exhibit variations a few min ahead of near-surface rainfall.

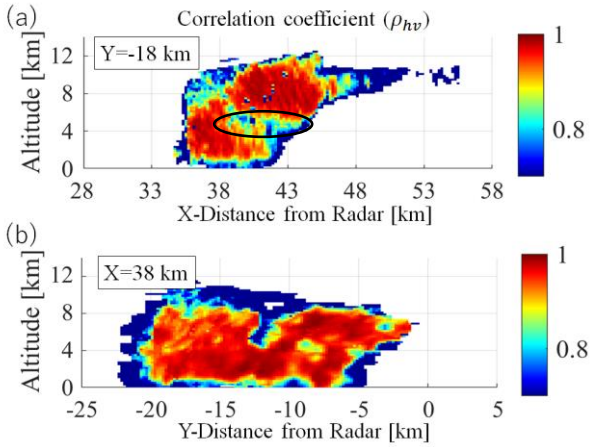

FIGURE 4. Vertical structure of the ρ_{hv} at the same time as Fig. 3. Panels (a) and (b) are slices of the XZ and YZ planes, respectively.

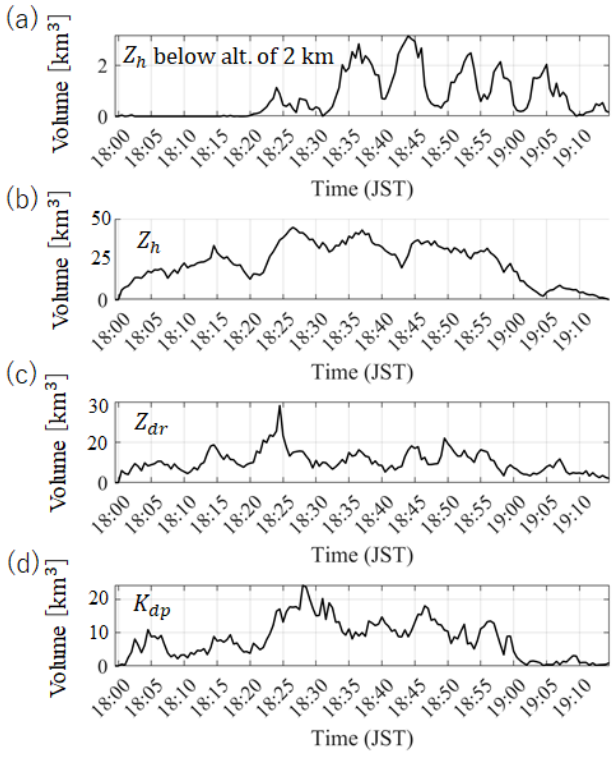

FIGURE 5. Temporal variation of the volume of Z_h below 2 km altitude, and Z_h, Z_{dr}, and K_{dp} at an altitude above the freezing level (4.5 km altitude) in panels (a), (b), (c), and (d), respectively.

Fig. 6 illustrates the lead-lag correlation coefficients and scatter plots of the temporal changes between the volume of Z_h, Z_{dr}, and K_{dp} above the freezing level and Z_h below 2 km altitude. In the scatter plot, the full volume scan data above the freezing level, which are corrected for time infomation using lead-lag time in panels (a,b,c-1), and Z_h volume below 2 km altitude are used. In panels (a-1) and (c-1), it was observed that the Z_h and K_{dp} volumes above the freezing level preceded the Z_h volume below 2 km altitude by 8.5 and 11.5 min, respectively, with correlation coefficients of 0.76 and 0.74, respectively. The coefficient of determination for the Z_h and K_{dp} volume was 0.55 or greater, as shown in panels (a-2) and (c-2), respectively. These findings indicate that Z_h and K_{dp} volumes above the freezing level can serve as valuable indicators for short-term predictions of near-surface rainfall volume. The previous studies reported that K_{dp} core, which is an area of enhanced positive K_{dp}, near and below melting layer appears to be associated with downdrafts in storms (e.g., [30]). Therefore, the K_{dp} core volume is considered suitable for estimating near-surface rainfall volume, though this study did not explicitly define the K_{dp} core. However, for Z_{dr} volume, despite a lead time of 20.5 min relative to surface rainfall, the correlation coefficient was a low value of 0.63. Additionally, the coefficient of determination for Z_{dr} was 0.40, which was lower than those for Z_h and K_{dp}. Several factors may account for this low correlation with surface rainfall. Z_{dr} tends to be more sensitive to very large liquid drops, possibly containing ice cores (drops exceeding 5 mm in diameter) or hail above the freezing level, in comparison to K_{dp} [16]. This distinction could contribute to the varying correlation coefficients between Z_{dr} and K_{dp}. Moreover, in this case,the absence of clearly observed Z_{dr} columns may have contributed to the lower correlation between Z_{dr} and near-surface rainfall.

Fig. 7 presents the time-altitude distribution of Z_h volume at > 45 dBZ, Z_{dr} volume at > 3 dB, and K_{dp} volume at > 3 °/km. In the Z_h and K_{dp} results of panels (a) and (c), three precipitation cores developed around 18:15:24, 18:30:24, and 18:40:24 and were clearly observed falling from high altitudes to the ground. These results indicate that increases or decreases in near-surface rainfall can be accurately predicted with a lead time of more than 8.5 min using the Z_h and K_{dp} volumes. However, in this case, the Z_{dr} volume did not clearly reveal the falling precipitation cores. In this case, the precipitation cores occur within a short time period and seems to temporally overlap each other. The temporal overlap of particles (hail, ice cry stal, rain, etc.) produced by different precipitation cores above the freezing level may have reduced the coefficient of determination for Z_{dr}.

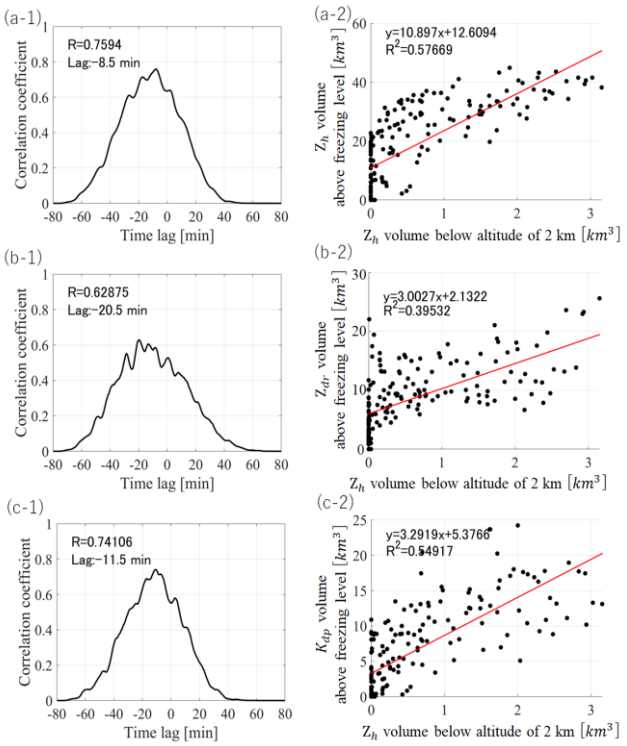

FIGURE 6. Lead-lag correlation coefficients and scatter plots of the temporal variations between (a) Z_h, (b) Z_{dr}, and (c) K_{dp} volume above freezing level and Z_h below 2 km altitude.

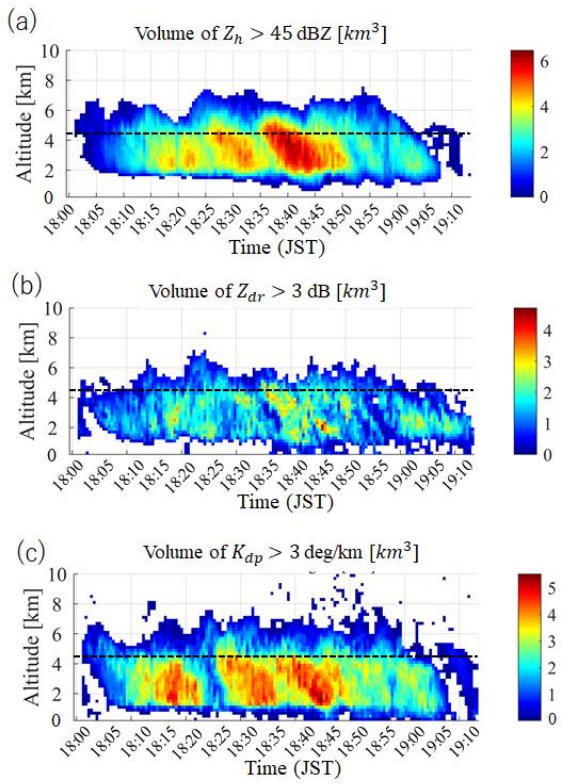

FIGURE 7. Time-altitude distribution of Z_h, Z_{dr}, and K_{dp} volume in panels (a), (b), and (c), respectively. Dashed line indicates the freezing level.

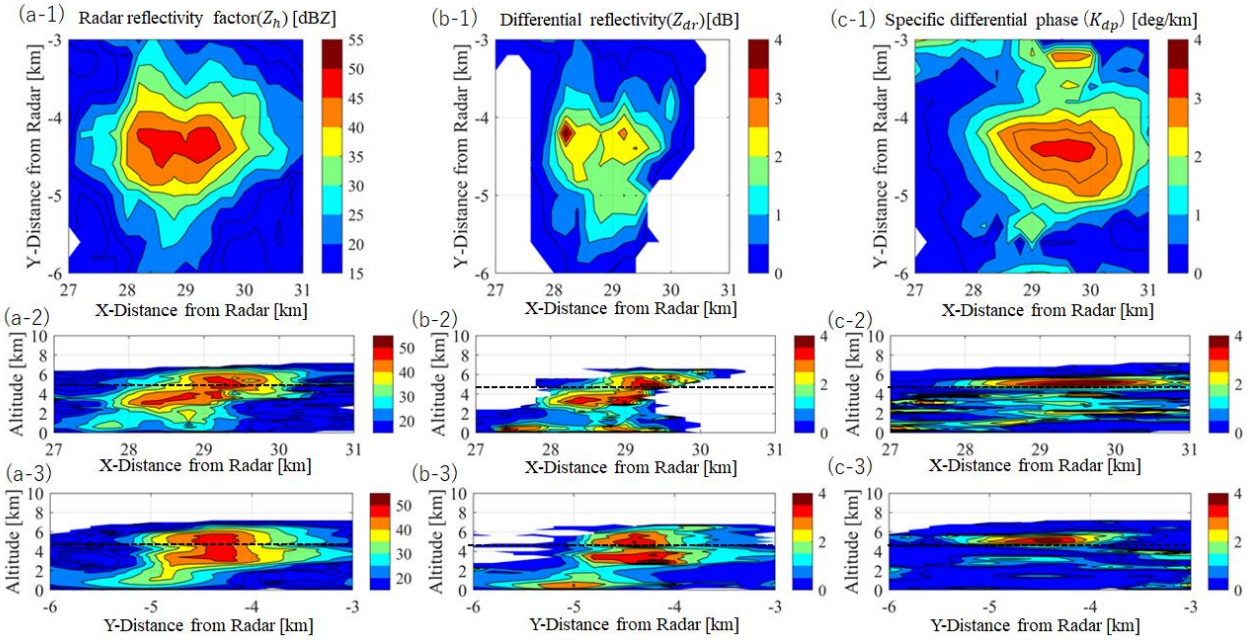

FIGURE 8. **3D distribution of the radar variables of Z_h, Z_{dr}, and K_{dp}. Panels (a), (b), and (c) show the maximum values of Z_h, Z_{dr}, and K_{dp} along a direction, respectively. The numbers 1, 2, and 3 indicate the maximum values across the vertical and horizontal direction. The dashed line indicates the freezing level.**

B. CASE 2

Case 2's storm was observed on August 22, 2020, from 18:00:24 to 18:35:24 (JST). In Fig. 8, the 3D distribution of radar variables Z_h, Z_{dr}, and K_{dp} using DP-PAWR at 18:14:54 is presented. The horizontal extent of the storm spanned 2–3 km, as evident in panel (a-1). When compared with case 1, the storm in case 2 was notably smaller. Precipitation cores formed at coordinates of 29 km (x) and -4.5 km (y). The vertical structure of Z_h, Z_{dr}, and K_{dp} did not reveal a melting layer signature around the freezing level, as indicated in panels (a-2,3), (b-2,3), and (c-2,3). The echo top at 45 dBZ was situated at an altitude of 6 km. Even with weak convective activity, DP-PAWR clearly captured the precipitation core.

Fig. 9 illustrates the vertical structure of ρ_{hv} at the same time as Fig. 8. Panels (a) and (b) provide slices of the XZ and YZ planes at Y coordinates of -4.5 km and X coordinates of 28.5 km, respectively. In case 2, it is difficult to define the melting layer from Fig. 9. However, because case 1 and 2 were observed at almost the same time, we also used the melting layer altitude of 4.5 km obtained in case 2.

In Fig. 10, the temporal changes in the volume of Z_h below 2 km altitude, and Z_h, Z_{dr}, and K_{dp} above the freezing level, are displayed. Panel (a) reveals an increase in surface rainfall volume from 18:18:24 to 18:25:24, peaking at 18:22:24. In panels (b), (c), and (d), the Z_h, Z_{dr} and K_{dp} volumes above the freezing level exhibited an approximate lead time of 8 min in relation to near-surface rainfall. The peak values for these variables were recorded around 18:14:24.

Fig. 11 presents the lead-lag correlation coefficients and scatter plots depicting the temporal variations in radar full volume scan data between the volume of Z_h, Z_{dr}, and K_{dp} above the freezing level and Z_h below 2 km altitude. In panels (a-1), (b-1), and (c-1), the Z_h, Z_{dr} and K_{dp} volumes above the freezing level exhibited a lead time of 7–8 min compared to the volume of near-surface rainfall. Panels (a-2) and (b-2) reveal coefficients of determination for the Z_h and Z_{dr} volumes, exceeding 0.84, even with a smaller dataset due to the storm's short duration. These results underscore the usefulness of Z_h and Z_{dr} volumes above the freezing level as predictive indicators for near-surface rainfall volume. However, the coefficient of determination for the K_{dp} volume was slightly lower, registering a mere 0.47. As described in [13], K_{dp} is most strongly correlated with intense convection and may not effectively track moderate deep convection activity. In this case, the convective storms were generally small with weak convective activity, leading to a relatively lower

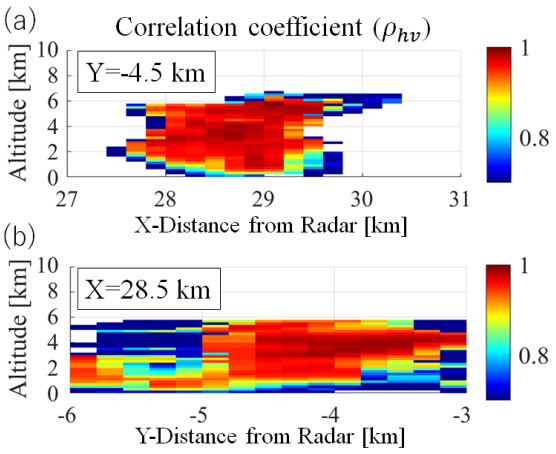

FIGURE 9. **Vertical structure of the ρ_{hv} at the same time as Fig. 8. Panels (a) and (b) are slices of the XZ and YZ planes.**

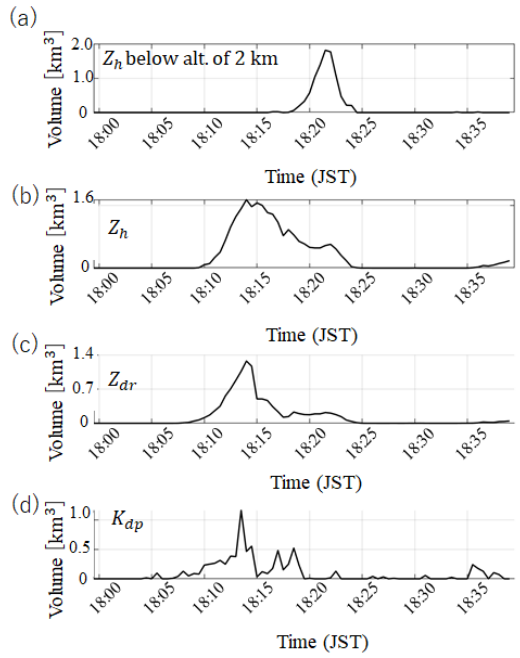

FIGURE 10. Temporal variation in the volume of Z_h below 2 km altitude, and Z_h, Z_{dr}, and K_{dp} at an altitude above the freezing level (4.5 km altitude) in panels (a), (b), (c), and (d), respectively.

coefficient of determination for the K_{dp} volume compared to the other variables.

Fig. 12 shows the time-altitude distribution of Z_h, Z_{dr}, and K_{dp} volume. In the Z_h and Z_{dr} results in panels (a) and (b), respectively, two precipitation cores were observed to develop and decline during the analysis period. DP-PAWR accurately observed the movement of precipitation cores in very small and temporally short storms by making 3D observations every 30 s. The precipitation cores descended from a high altitude towards the ground for approximately 8 min prior to the near-surface rainfall beginning. For Z_{dr}, the precipitation cores were clearly observed, indicating that the two cores generated in case 2 could be separated in time. These two points may have resulted in a different result from case 1.

In the case of the K_{dp} result, the descent of the precipitation cores was distinctly observed. However, it was noted that the K_{dp} volume was not observed for the second core, which resulted in very little near-surface rainfall. These findings indicate that Z_h and Z_{dr} volumes above the freezing level are valuable for quantitatively predicting the volume of near-surface rainfall in case 2. While the K_{dp} volume above the freezing level may not be conducive to predicting near-surface rainfall volume quantitatively in very small storms, it can effectively detect developing precipitation cores in advance. For K_{dp} volume in this case, optimizing the threshold value may improve the accuracy of ground rainfall estimation, but since the objective of this paper is to predict heavy rainfall disasters using a simple threshold, changing the threshold value is a subject for future study.

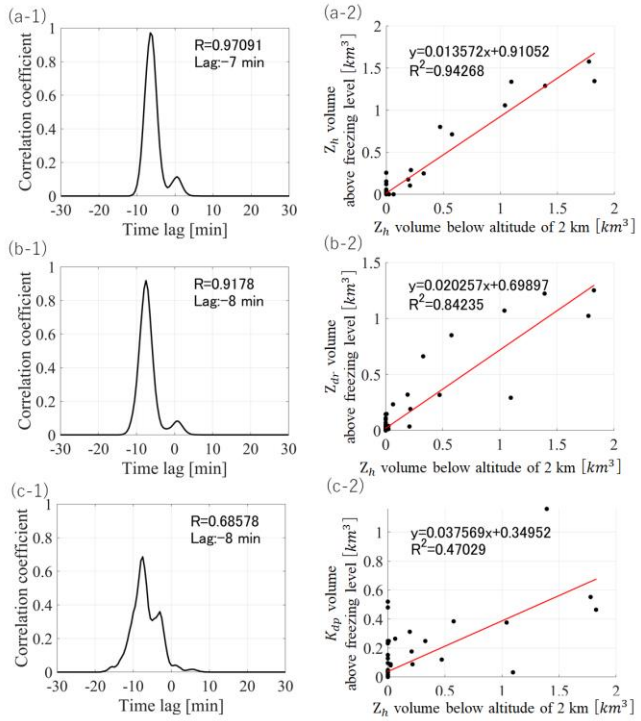

FIGURE 11. Lead-lag correlation coefficients and scatter plots of the temporal variations in between the volume of (a) Z_h, (b) Z_{dr}, and (c) K_{dp}

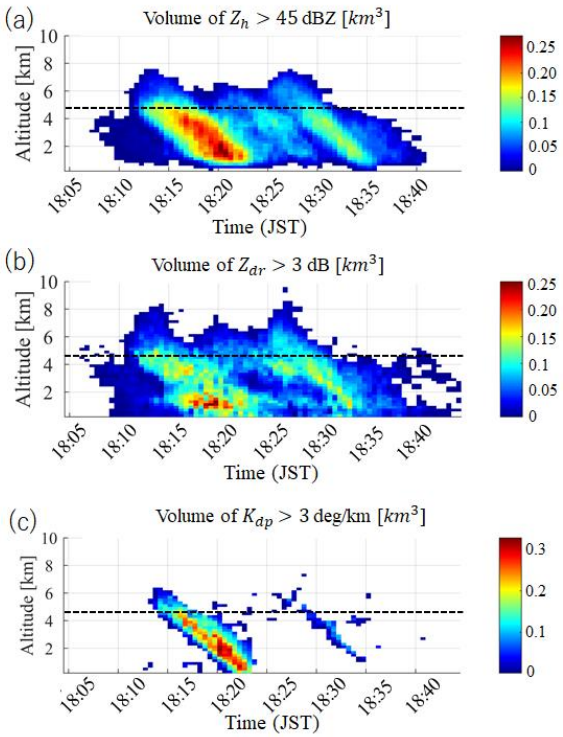

FIGURE 12. Time-altitude distribution of Z_h volume, Z_{dr} volume and K_{dp} volume in panels (a), (b), and (c), respectively. Dashed line indicates the freezing level.

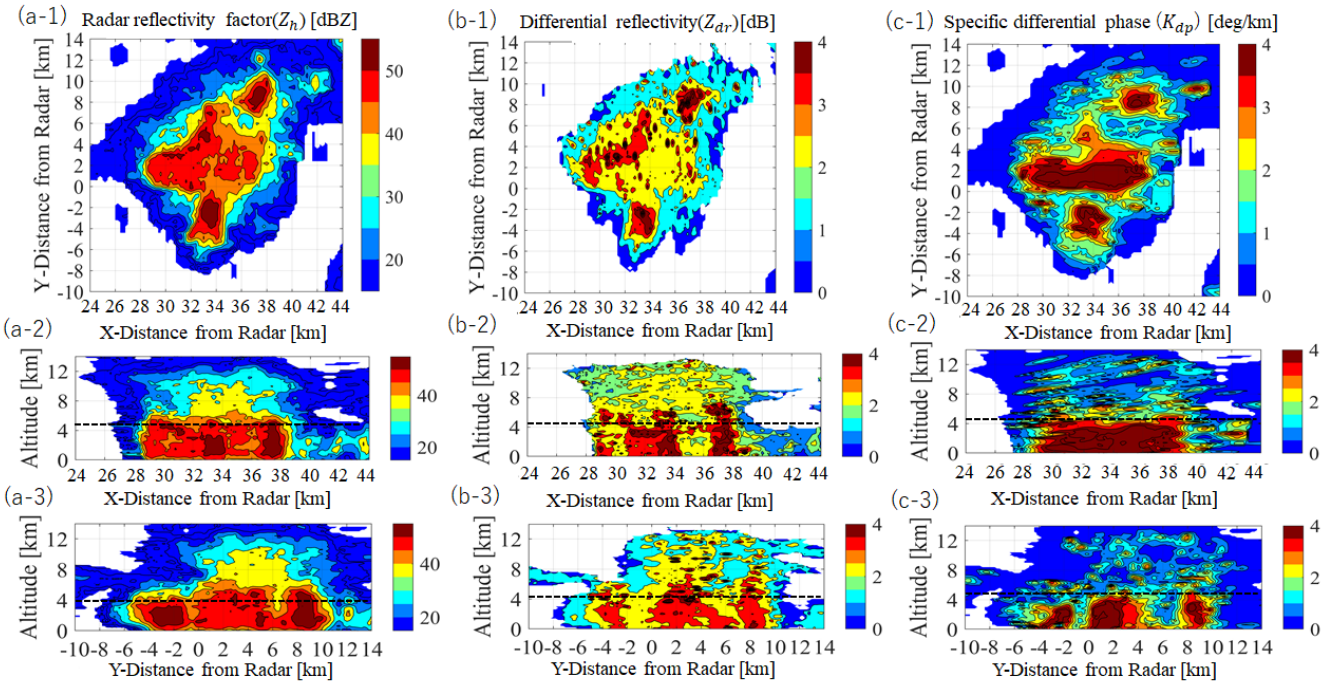

FIGURE 13. **3D distribution of the radar variables of Z_h, Z_{dr}, and K_{dp}. Panels (a), (b), and (c) show the maximum values of Z_h, Z_{dr}, and K_{dp} along a direction, respectively. The numbers 1, 2, and 3 indicate the maximum values across the vertical and horizontal direction. The dashed line indicates the freezing level.**

B. CASE 3

The storm in case 3 was observed on July 30, 2021 from 11:40:33 to 14:35:33 (JST). Fig. 13 shows the 3D distribution of radar variables at 13:31:33. The scale of the storm was about a dozen kilometers horizontally. The Z_h shown in panel (a) indicate that there are at least two or more precipitation cores within the analysis area. The echo top of 45 dBZ was situated at an altitude of 7 km. The vertical structure of Z_h, Z_{dr}, and K_{dp} did not reveal a melting layer signature around the freezing level, as indicated in panels (a-2,3), (b-2,3), and (c-2,3).

Fig. 14 shows the vertical structure of the ρ_{hv}. It is difficult to define the melting layer from the distribution of the ρ_{hv} as in case 2. In this case, we decided to use the melting layer altitude of 4.7 km from the radiosonde data as shown in Fig. 2(b).

Fig. 15 indicates the temporal changes in the volume of the radar variables. Panel (a) reveals an increase in near-surface rainfall volume from 11:50:33 to 13:10:33, peaking at 12:43:33. In panels (b), (c), and (d) the Z_h, Z_{dr}, and K_{dp} volumes above

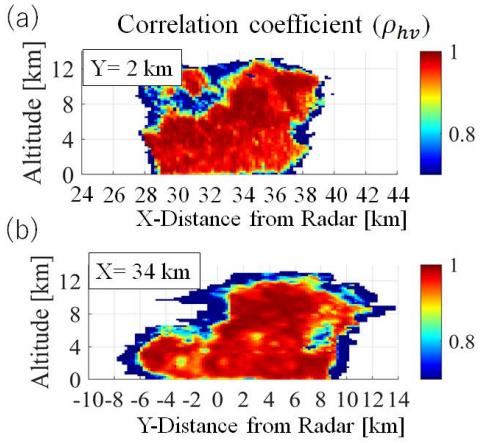

FIGURE 14. **Vertical structure of the ρ_{hv} at the same time as Fig. 13. Panels (a) and (b) are slices of the XZ and YZ planes at Y of 2 km and X of 34 km, respectively.**

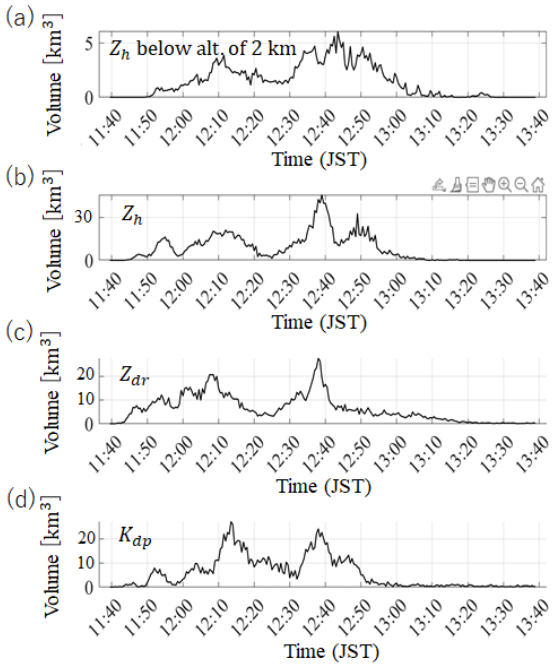

FIGURE 15. **Temporal variation in the volume of Z_h below 2 km altitude, and Z_h, Z_{dr}, and K_{dp} at an altitude above the freezing level (4.7 km altitude) in panels (a), (b), (c), and (d), respectively.**

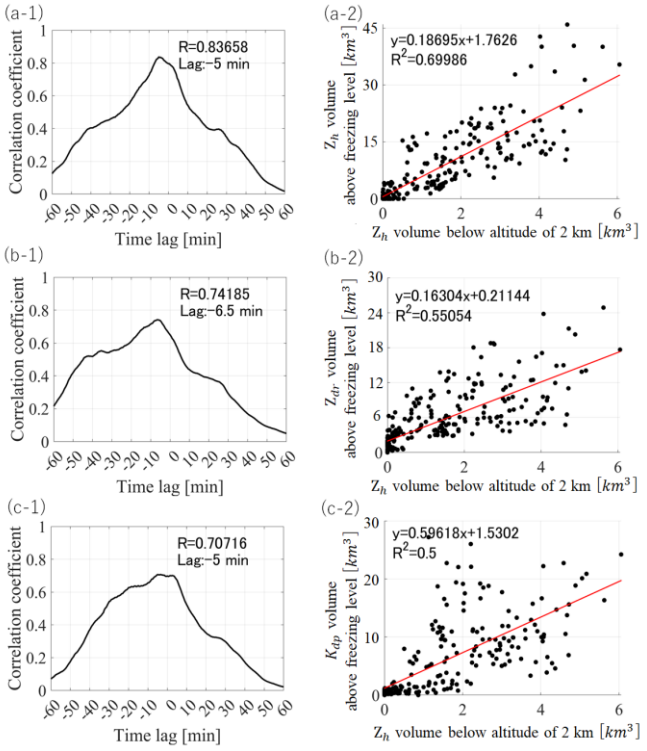

FIGURE 16. **Lead-lag correlation coefficients and scatter plots of the temporal variations in the radar volumetric data between (a) Z_h, (b) Z_{dr}, and (c) K_{dp} above freezing level and Z_h velow 2 km altitude.**

the freezing level exhibited an approximate lead time of 5 min in relation to near-surface rainfall.

Fig. 16 shows the lead-lag correlation coefficients and scatter plots depicting the temporal variations. In panels (a-1), (b-1), and (c-1), the $Z_h, Z_{dr},$ and K_{dp} volumes above the freezing level exhibited a lead time greater than 5 min compared to the volume of near-surface rainfall. The coefficients of determination are also greater than 0.5. In this case, all variables showed precise accuracy in predicting near-surface rainfall.

Fig. 17 shows the time-altitude distribution of the Z_h, Z_{dr}, and K_{dp} volume. In all variables, we can clearly observe a strong precipitation core that occurred around 12:43. The DP-PAWR accurately observed the movement of precipitation cores from high to low altitude.

The results of Z_h and K_{dp} are similar to case 1. Meanwhile, Z_{dr} had a greater coefficient of determination than case 1. Unlike case 1, the precipitation cores are developing, concentrated at the time 12:43 as shown in Fig. 17. In this case, no temporal overlap due to multiple precipitation cores occurring in a short period of time was observed, which may have avoided the complexity of the generation and distribution of particles at high altitude. Furthermore, the Z_{dr} observations clearly showed the precipitation core.Hence, this result in case 3 is also similar in trend to case 2. Finally, we have summarized the results in Table 2.

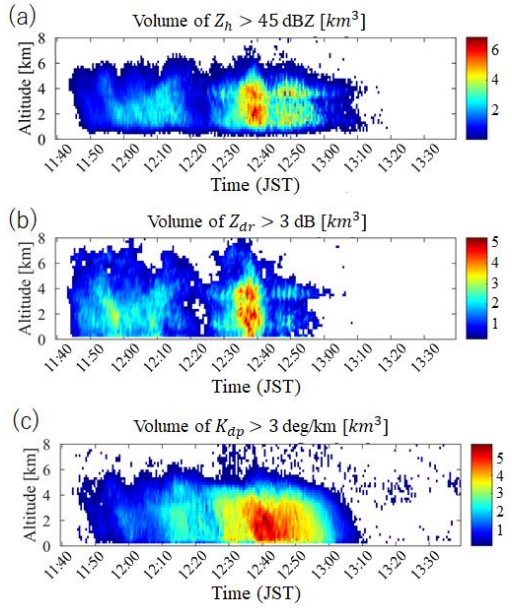

FIGURE 17. **Time-altitude distribution of Z_h volume, Z_{dr} volume and K_{dp} volume in panels (a), (b), and (c), respectively. Dashed line indicates the freezing level.**

IV. CONCLUSIONS

This study aimed to explore the relationship between the volume of several radar variables (Z_h, Z_{dr}, and K_{dp}) above the freezing level and near-surface rainfall using DP-PAWR for three distinct summer convective storms. The research delved into the quantitative predictability of near-surface rainfall volume based on these radar variables.

In the case of heavy convective storms, as described in case 1, it was observed that the Z_h and K_{dp} volumes above the freezing level had a lead time of over 8.5 min in relation to near-surface rainfall volume, with a coefficient of determination exceeding 0.55. The Z_{dr} volume exhibited a weaker correlation with near-surface rainfall in this scenario.

For the small-scale convective storm in case 2, the Z_h and Z_{dr} volumes proved highly effective in predicting surface rainfall volume, with a lead time exceeding 7 minutes and a

TABLE 2
LEAD-LAG TIME AND COEFFICIENT OF DETERMINATION FOR THE SURFACE RAINFALL.

		Lead-lag [min]	coefficient of determination
Case 1 (heavy convective +multicore)	Z_h	-8.5	0.58
	Z_{dr}	-20.5	0.40
	K_{dp}	-11.5	0.55
Case 2 (weak convective)	Z_h	-7.0	0.94
	Z_{dr}	-8.0	0.84
	K_{dp}	-8.0	0.47
Case 3 (heavy convective +multicore)	Z_h	-5.0	0.70
	Z_{dr}	-6.5	0.55
	K_{dp}	-5.0	0.50

coefficient of determination surpassing 0.84. However, the K_{dp} volume above the freezing level was found to be less reliable in forecasting surface rainfall volume due to its limited sensitivity in this context of a small-scale convective storm.

For heavy convective storms in cases 3, all variables showed the potential to predict near-surface rainfall with a coefficient of determination of 0.5 or better accuracy at least 5 min lead time.

These results show that by combining the 30-s full volume scan data observed by DP-PAWR, it is possible to quantitatively predict surface rainfall for various types of developing convective storms, ranging in time from 5 minutes to around 11 minutes. This research also holds promise for predicting precipitation-related flash flooding. In the future, an increase in DP-PAWR production in Japan is expected. Conducting statistical analyses across numerous storm cases is anticipated to enhance the accuracy of quantitative near-surface rainfall forecasting by identifying combinations of high-altitude volume of several radar variables tailored to the scale of convective activity.

ACKNOWLEDGMENTS

The authors thank Dr. S. Satoh from the National Institute of Information and Communications Technology (NICT) for providing the radar data of the DP-PAWR. The radio sonde data are archived by the Japan Meteorological Agency and are available at http://www.jma.go.jp/jma/index.html. The authors also thank the people from Toshiba Corporation for their valuable comments about the hardware in the DP-PAWR. The data for the DP-PAWR used in this study are available on request (hkikuchi@uec.ac.jp).

REFERENCES

[1] A. Nekrasov et al., "On Sea Ice/Water Discrimination by Airborne Weather Radar," in IEEE Access, vol. 8, pp. 120916-120922, 2020, doi: 10.1109/ACCESS.2020.3006617.

[2] Y. Umeyama, J. L. Salazar-Cerreno and C. Fulton, "UAV-Based Antenna Measurements for Polarimetric Weather Radars: Probe Analysis," in IEEE Access, vol. 8, pp. 191862-191874, 2020, doi: 10.1109/ACCESS.2020.3027779.

[3] B. A. Nunna and V. K. Kothapudi, "A Novel C/X-Band Linear Polarized Conformal Shared Aperture Antenna Array for Spaceborne SAR Applications," in IEEE Access, vol. 11, pp. 101045-101054, 2023, doi: 10.1109/ACCESS.2023.3315117.

[4] R. J. Doviak and D. S. Zrnić, "Doppler radar and weather observations. Courier Dover," *Publications*, 562 pp. 1993.

[5] D. S. Zrnić and A. V. Ryzhkov, "Polarimetry for weather surveillance radars," *Bull. Am. Meteorol. Soc.*, vol. 80, no. 3, pp. 389–406, 1999.

[6] V. N. Bringi and V. Chandrasekar, *Polarimetric Doppler Weather Radar: Principles and Applications*. Cambridge University Press, 2001, 664 pp.

[7] M. R. Kumjian, "Principles and applications of dual-polarization weather radar. Part I: Description of the polarimetric radar variables," *J. Oper. Meteorol.*, vol. 1, no. 19, pp. 226–242, 2013.

[8] M. R. Kumjian, "Principles and applications of dual-polarization weather radar. Part II: Warm-and cold-season applications," *J. Oper. Meteorol.*, vol. 1, no. 19, pp. 243–264, 2013.

[9] A. J. Illingworth, J. W. F. Goddard, and S. M. Cherry, "Polarization radar studies of precipitation development in convective storms," *Q. J. R. Meteorol. Soc.*, vol. 113, no. 476, pp. 469–489, 1987.

[10] I. J. Caylor and A. J. Illingworth, "Radar observations and modelling of warm rain initiation," *Q. J. R. Meteorol. Soc.*, vol. 113, no. 478, pp. 1171–1191, 1987.

[11] A. V. Ryzhkov, V. B. Zhuravlyov, and N. A. Rybakova, "Preliminary results of X-band polarization radar studies of clouds and precipitation," *J. Atmos. Oceanic Technol.*, vol. 11, no. 1, pp. 132–139, 1994.

[12] J. Brandes J. Vivekanandan, J. D. Tuttle, and C. J. Kessinger, "A Study of Thunderstorm Microphysics with Multiparameter Radar and Aircraft Observations," *Monthly Weather Review*, vol. 123, no. 11, pp. 3129–3143, 1995.

[13] M. van Lier-Walqui, A. M. Fridlind, A. S. Ackerman, S. Collis, J. Helmus, D. R. MacGorman, K. North, P. Kollias, and D. J. Posselt, "On polarimetric radar signatures of deep convection for model evaluation: Columns of specific differential phase observed during MC3E," *Monthly Weather Review*, vol. 144, no. 2, pp. 737-758, 2016.

[14] M. L. Loney, D. S. Zrnić, J. M. Straka, and A. V. Ryzhkov, "Enhanced polarimetric radar signatures above the melting level in a supercell storm," *Journal of Applied Meteorology*, vol. 41, no. 12, pp. 1179–1194, 2002.

[15] M. R. Kumjian and A. V. Ryzhkov, "Polarimetric signatures in supercell thunderstorms," *Journal of Applied Meteorology and Climatology*, vol. 47, no. 7, pp. 1940–1961, 2008.

[16] M. R. Kumjian, A. P. Khain, N. Benmoshe, E. Ilotoviz, A. V. Ryzhkov, and V. T. J. Phillips, "The anatomy and physics of ZDR columns: Investigating a polarimetric radar signature with a spectral bin microphysical model," *Journal of Applied Meteorology and Climatology*, vol. 53, no. 7, pp. 1820–1843, 2014.

[17] J. C. Snyder, H. B. Bluestein, V. Venkatesh, and S. J. Frasier, "Observations of polarimetric signatures in supercells by an X-band mobile Doppler radar," *Monthly Weather Review*, vol. 141, no. 1, pp. 3–29, 2013.

[18] T. Maesaka, M. Maki, K. Iwanami, S. Tsuchiya, K. Kieda, and A. Hoshi, "Operational rainfall estimation by X-band MP radar network in MLIT, Japan". *35th conference on Radar Meteorology*, Pittsburgh, PA, Amer. Meteor. Soc., pp. 11.142, 2011.

[19] M. Maki, S. Park, V. N. Bringi, "Effect of natural variations in rain drop size distributions on rain rate estimators of 3 cm wavelength polarimetric radar," *J. Meteorol. Soc. Jpn.*, vol. 83, pp. 871–893, 2005.

[20] D. S. Zrnic, J. F. Kimpel, D. E. Forsyth, A. Shapiro, G. Crain, R. Ferek, J. Heimmer, W. Benner, F. T. J. McNellis, and R. J. Vogt, "Agile-beam phased array radar for weather observations," *Bulletin of the American Meteorological Society*, vol. 88, no. 11, pp. 1753–1766, 2007.

[21] P. L. Heinselman, D. L. Priegnitz, K. L. Manross, T. M. Smith, and R. W. Adams, "Rapid sampling of severe storms by the national weather radar testbed phased array radar," *Weather Forecasting*, vol. 23, no. 5, pp. 808–824, 2008.

[22] C. Wu, L. Liu, X. Liu, G. Li, and C. Chen, "Advances in Chinese dual-polarization and phased-array weather radars: Observational analysis of a supercell in Southern China," *Journal of Atmospheric and Oceanic Technology*, vol. 35, no. 9, pp. 1785–1806, 2018.

[23] M. Weber, et al. , "Towards the Next Generation Operational Meteorological Radar," *Bulletin of the American Meteorological Society*, vol. 102, no. 7, pp. E1357-E1383, 2021.

[24] R. Palmer, et al., "A Primer on Phased Array Radar Technology for the Atmospheric Sciences," *Bulletin of the American Meteorological Society,* vol. 103, no. 10, pp. E2391-E2416, 2022.

[25] D. Schvartzman, "Mitigation of Wind Turbine Clutter With Digital Phased Array Radar," in IEEE Access, vol. 11, pp. 12911-12924, 2023, doi: 10.1109/ACCESS.2023.3242910.

[26] H. Kikuchi, Y. Hobara and T. Ushio, "Compressive Sensing to Reduce the Number of Elements in a Linear Antenna Array With a Phased Array Weather Radar," *IEEE Transactions on Geoscience and Remote Sensing*, vol. 60, pp. 1-10, 2022, Art no. 5111210, doi: 10.1109/TGRS.2022.3152998.

[27] D. Kitahara, H. Kuroda, A. Hirabayashi, E. Yoshikawa, H. Kikuchi and T. Ushio, "Nonlinear Beamforming Based on Group-Sparsities of Periodograms for Phased Array Weather Radar," in IEEE Transactions on Geoscience and Remote Sensing, vol. 60, pp. 1-19, 2022, Art no. 4106819, doi: 10.1109/TGRS.2022.3154118.

[28] H. Kikuchi, T. Suezawa, T. Ushio, N. Takahashi, H. Hanado, K. Nakagawa, M. Osada, T. Maesaka, K. Iwanami, K. Yoshimi, F. Mizutani, M. Wada, and Y. Hobara, "Initial observations for precipitation cores with X-band dual polarized phased array weather radar" *IEEE Transactions on Geoscience and Remote Sensing*, vol. 58, no. 5, pp. 3657-3666, May 2020.

[29] K. Asai, H. Kikuchi, T. Ushio, and Y. Hobara, "Validation of X-band multiparameter phased-array weather radar by comparing data from Doppler weather radar with a parabolic dish antenna," *J. Atmos. Ocean. Technol.*, vol. 38, no. 9, pp. 1561-1570, 2021.

[30] M. R. Kumjian, Z. J. Lebo, and A. M. Ward, "Storms producing large accumulations of small hail," *J. Appl. Meteor. Climatol.*, vol. 58, pp. 341–364, 2019, https://doi.org/10.1175/JAMC-D-18-0073.1

[31] M. R. Kumjian, "Principles and Applications of Dual-Polarization Weather Radar. Part II: Warm- and Cold-Season Applications." *Journal of Operational Meteorology*, vol. 1(20), pp. 243-264, 2013.

[32] M. L. Loney, D. S. Zrnić, J. M. Straka, and A. V. Ryzhkov "Enhanced Polarimetric Radar Signatures above the Melting Level in a Supercell Storm", *Journal of Applied Meteorology and Climatology*, vol. 41, pp. 1179–1194, 2002.

[33] M. R Kumjian, A. V. Ryzhkov, V. M. Melnikov, and T. J. Schuur, "Rapid-Scan Super-Resolution Observations of a Cyclic Supercell with a Dual-Polarization WSR-88D", *Mon. Wea. Rev.*, vol. 138, pp. 3762–3786, 2010.

HIROSHI KIKUCHI (M'14) received the B.S. degree from Department of

Engineering, Doshisha University, Kyoto, Japan, in 2008 and the M.S., and Ph.D. degrees from the Division of Electrical, Electronic and Information Engineering, Osaka University, Suita, Japan, in 2010 and 2013, respectively. He joined the Division of Electrical, Electric and Information Engineering, Osaka University as a Specially Appointed Researcher in 2013. In 2017, he was a Research Assistant Professor at Tokyo Metropolitan University.In 2018, he joined the University of Electro Communications, where he is currently an Assistant Professor. His research specialties are the remote sensing for an atmospheric electricity with space-borne platforms, and the weather radar remote sensing and a development of the radar system.

YASUHIDE HOBARA received the B.S., M.S. and Ph.D. degrees in

Electrical Engineering from The University of Electro-Communications (UEC), Japan, in 1991, 1994, and 1997, respectively. Following his graduation from the UEC, he worked at Institute of Applied Physics (Russia), Earth Observation Research Center, JAXA, Laboratoire de Physique et Chimie de l'Environnement et de l'Eespace ?CNRS (France), Swedish institute of space physics (Sweden), The University of Sheffield (United Kingdom), and Tsuyama National College of Technology (Japan). He joined the Department of Computer and Network Engineering, Engineering, Graduate School of Informatics and Engineering in UEC in 2009 where he is currently a Professor. Terrestrial and space electromagnetic environment is his main field of research including space plasma science, Atmospheric Electricity and seismo-electromagnetics.

TOMOO USHIO (M'02) received the B.S, M.S., and Ph.D. degree in

electrical engineering from Osaka University in 1993, 1995, 1998, respectively. He was with the Global Hydrology and Climate Center, Huntsville AL USA as a Postdoctorate Researcher from 1998 to 2000. In 2000, he joined the Department of Aerospace Engineering, Osaka Prefecture University. In 2006, he was with the Department of Electrical, Electronic and Information Engineering, Osaka University Japan as an associate professor. Since 2019, he has been a professor in Osaka University. His research specialties are radar-based remote sensing, passive and active remote sensing of atmosphere from space borne platforms, and atmospheric electricity.